Nanoscale

PAPER

Check for updates

Strategies to initiate and control the nucleation behavior of bimetallic nanoparticles†

Gopi Krishnan, [iD] *[a,b] Sytze de Graaf,[a] Gert H. ten Brink,[a] Per O.Å. Persson, [iD] [c]
Bart J. Kooi[a] and George Palasantzas[a]

In this work we report strategies to nucleate bimetallic nanoparticles (NPs) made by gas phase synthesis of elements showing difficulty in homogeneous nucleation. It is shown that the nucleation assisted problem of bimetallic NP synthesis can be solved *via* the following pathways: (i) selecting an element which can itself nucleate and act as a nucleation center for the synthesis of bimetallic NPs; (ii) introducing H_2 or CH_4 as an impurity/trace gas to initiate nucleation during the synthesis of bimetallic NPs. The latter can solve the problem if none of the elements in a bimetallic NP can initiate nucleation. We illustrate the abovementioned strategies for the case of Mg based bimetallic NPs, which are interesting as hydrogen storage materials and exhibit both nucleation and oxidation issues even under ultra-high vacuum conditions. In particular, it is shown that adding H_2 in small proportions favors the formation of a solid solution/alloy structure even in the case of immiscible Mg and Ti, where normally phase separation occurs during synthesis. In addition, we illustrate the possibility of improving the nucleation rate, and controlling the structure and size distribution of bimetallic NPs using H_2/CH_4 as a reactive/nucleating gas. This is shown to be associated with the dimer bond energies of the various formed species and the vapor pressures of the metals, which are key factors for NP nucleation.

Introduction

Bimetallic nanoparticles (NPs) have attracted much interest due to their interesting properties and wide range of application areas *e.g.* catalysts, plasmonics, magnetism *etc*.[1,2] The synthesis of bimetallic NPs with controlled size and shapes has been reported to date by different routes.[1–6] Recently, a gas-phase synthesis method based on DC/RF magnetron sputtering showed a significant improvement in bimetallic NP synthesis with controlled structures and compositions.[7–11] Moreover, this method is more promising compared to other physical and chemical methods due to the single step generation of high purity NPs. Although fine-tuning of bimetallic NPs with different structural motifs and sizes is very well established and reported for noble and some transition metals,[9,10,12,13] it remains a challenge to extend this approach

to alkali and alkaline earth metals. This is because these metals with a low reduction potential readily react with oxygen and water. Moreover, insufficient information on the mono and/or bimetallic NP nucleation mechanisms is a major drawback in understanding the formation process of bimetallic NPs.

The nucleation mechanism can be either homogeneous or heterogeneous depending on the bimetallic elements used, and the presence of trace impurities/reactive adsorbates during synthesis. In general, the environmental conditions play a major role in the formation and growth of nuclei, and in the size, shape and purity of the produced NPs as well.[14,15] Generally, trace impurities, *e.g.* O_2 present in the sputtering gas/chamber, can play three different roles, independently starting from the nucleation, growth, and oxidation of NPs depending on the concentration of O_2 present.[14,15] Nevertheless, the effect of impurities (*e.g.*, O_2, H_2O) on the nucleation behavior has hardly been studied in detail. Generally, homogeneous nucleation is difficult to initiate for all the mono and bimetallic syntheses, because it has a high-energy nucleation barrier compared to heterogeneous nucleation. Moreover, one of the major problems is to differentiate the presence of impurities playing a role during nucleation as compared to homogeneous nucleation, since a low concentration of impurities can successfully produce M-X species/nuclei that can act as a nucleation center for NP growth.

[a]Zernike Institute for Advanced Materials, University of Groningen, Nijenborgh 4, 9747 AG Groningen, The Netherlands. E-mail: gopi.k.krish@gmail.com
[b]Center for Nanosciences and Molecular medicine, Amrita University, Kochi, Kerala, 682041 India
[c]Thin Film Physics Division, Department of Physics Chemistry and Biology (IFM), Linköping University, SE-581 83 Linköping, Sweden
†Electronic supplementary information (ESI) available: Experimental details including target arrangement, a schematic of the gas phase synthesis setup and EDX information. See DOI: 10.1039/c7nr00916j

Moreover, the presence of impurities during NP production and their role in the NP nucleation process are only realized after the complete depletion of impurities. This is manifested as a termination of the nucleation process, affecting also the nanoparticle production rate. Furthermore, once the impurities start to deplete in time, the concentration of impurities becomes so low that it cannot favor the formation of nuclei. As a result the synthesis of NPs completely stops, unless it proceeds further with homogeneous nucleation.

Recent reports on Ti, Co and Al NP nucleation show that adding a small amount of oxygen as an impurity/adsorbate or exposing the NP production system to an open atmosphere can favor NP nucleation,[16–19] when homogeneous nucleation is difficult to start. Hence, it becomes also crucial to understand the effect of impurities on the composition, structure, and purity of the produced NPs, in addition to solving the nucleation problem. Therefore one must find the right balance between the impurity concentrations required for initiating and producing good purity NPs. For example, in the case of O_2 as an impurity, NP production without involving the formation of metal oxide/bimetallic oxide is a key to solve the nucleation problem, in a scenario where homogeneous nucleation is completely blocked. Elements like Mg, which have a high affinity for oxygen, will be very difficult to synthesize using the addition of O_2 since there are high chances of producing MgO NPs,[20–22] as well as it will favor void formation in the NPs due to the Kirkendall effect associated with oxidation.[20,21] Hence, using O_2 will not be useful for most elemental/bimetallic NP syntheses, when the metals have high affinity to oxygen.

Therefore, in this work we discuss exclusively the possibility of initiating and controlling the nucleation behavior of bimetallic nanoparticles by introducing hydrogen and methane. We also show the possibility and merits of combining two different elements, where one element can be used to initiate the nucleation in bimetallic NPs. In particular, we have explored this possibility for magnesium based bimetallic NPs, which are interesting for hydrogen storage materials.

Fig. 1 Bright-field TEM image of MgTi core shell (a, c) NPs produced at 0.250 A using ($\frac{1}{2}$Mg + $\frac{1}{2}$Ti) section target without the addition of H_2 trace gas.(b, d) MgTi solid solution NPs synthesized using H_2 addition. (e, f) Diffraction patterns of Mg–Ti NPs with and without H_2, respectively.

Results and discussion

Fig. 1(a and c) shows a bright field TEM image of MgTi alloy nanoparticles synthesized at 0.250 A, using a section target of Mg and Ti. The size range of the particle is approximately ~12–35 nm. The MgTi NPs produced show a core shell structure with Ti as a core and Mg as a shell. This observation is similar to that for MgNi and MgCu NPs produced under the same conditions of 0.250 A and gas flow, where Ni and Cu act as nuclei for the formation of NPs.[11] Also considering the difficulty of Mg nucleation, it is more valid that the other element added acts as a nucleus for Mg growth. Finally, in comparison with MgNi and MgCu NPs, we can confirm that Ti act as nuclei for Mg growth. Moreover, segregation of Ti is excluded as one of the reasons for the core shell structure formation. This is because it has already been reported in the case of MgTi thin films produced by sputtering and supported
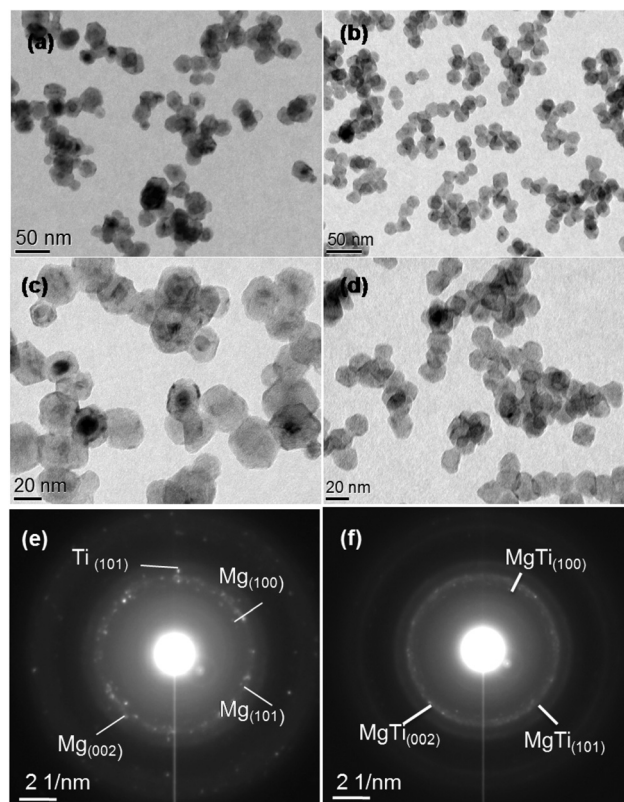
by DFT calculations that Ti segregates in the form of nanoclusters in an Mg rich composition.[23] These clusters are also distributed throughout the Mg matrix and Ti does not completely phase separate. Moreover, we reported earlier that Ti act as nuclei for the formation of Mg NPs, since Mg has nucleation difficulty and prefers always to grow on Ti.[21]

However, after the prolonged duration of NP synthesis for 15 minutes, the deposition rate/yield (NPs collected on the substrate) decreases rapidly and comes to a complete halt, as observed from quartz crystal monitor (QCM) data. Restarting the synthesis procedure did not show any improvement in favoring NP nucleation and the NP synthesis could not be initiated again. This confirms that the presence of impurities in the target or in the ambient environment during synthesis plays an important role in the nucleation of Ti. Simultaneously, the impurity/adsorbate that initiated the nucleation has been consumed during the course of the synthesis, thereby affecting the continuous nucleation and production of NPs. Fig. 1(c) also confirms that Mg does not nucleate on its own and always prefers to grow around Ti, as observed for most of the produced NPs. Particularly, O_2 can act as an impurity/adsorbate in the formation of TiO_x species that can further act as nucleation centers for Ti nucleus formation, but as the concentration of O_2 decreases, the formation of

TiO$_x$ species stops which cancels further nucleation of Ti cores.

Our experiments also confirm that the NPs produced at different intervals of the same deposition show rather different sizes and are inhomogeneous, indicating the effect of continuous O$_2$ depletion during the synthesis process. To sustain the nucleation process we introduced H$_2$ gas as a trace gas to initiate and sustain the synthesis of NPs. Fig. 1(b) & (d) show TEM images of MgTi NPs synthesized using H$_2$. The NPs' size varies between ~12–19 nm and confirms a narrow size distribution for the MgTi NPs shown in Fig. 1(b) & (d). These NPs have a composition of 87 ± 2 at% Mg and 13 ± 2 at% Ti as measured by EDX. The produced MgTi NPs exhibit a homogeneous morphology, which indicates a solid solution of Mg and Ti, in contrast to the core–shell morphology observed in Fig. 1(a) & (c) without H$_2$ addition. The diffraction pattern shown in Fig. 1(f) confirms that it is indeed a HCP based solid solution of MgTi, as the measured interplanar distances of MgTi d_{100}, d_{002} and d_{101} are 0.273 ± 0.002 nm, 0.256 ± 0.002 nm, 0.240 ± 0.002 nm, respectively. Although these values deviate from those of pure Mg which are d_{100} = 0.277, d_{002} = 0.260, and d_{101} = 0.245 nm, they agree with the lattice spacing of a HCP solid solution of MgTi.

Our results confirm that the Ti composition varying from 0–15 at% in MgTi NPs always results in a HCP based solid solution similar to MgTi thin films and MgTi particles produced by ball milling. Nucleation of NPs did not cease while H$_2$ was introduced into the NP production zone. By the application of H$_2$ during the growth process, the NPs produced and deposited at different intervals of the same deposition show a uniform composition and structure, unlike MgTi synthesis without H$_2$. The NPs shown in Fig. 1(a) & (c) and (b) & (d) are produced under the same conditions with the same target composition, while the morphologies are distinctly different, with a solid solution structure with H$_2$ and a core shell structure without H$_2$. This shows that H$_2$ introduction promotes the formation of a solid solution. In our previous work on MgNi, MgCu and MoCu NPs we have reported that a change in the thermal environment e.g. a change in plasma density (temperature) or Ar flow rate (cooling rate) during the synthesis conditions can form an alloy/solid solution structure for immiscible Mo–Cu.[7,11] Here, however, for MgTi, which is also immiscible, we show that the formation of a solid solution can be achieved by introducing H$_2$ without altering the plasma density and cooling rate. Moreover, MgTi NPs produced using hydrogen show a solid solution structure, in contrast to CH$_4$ as a trace gas and NPs produced without any trace gas under the same conditions of 0.250 A and Ar flow rate. This clearly demonstrates that the solid solution structure formation is not due to changes in the thermal environment. In addition, the MgTi nucleation issue without any trace gas does not allow the possibility of altering the thermal environment to observe any structural change. Finally, the presence of hydrogen during NP formation induces defects, which favor the formation of solid solution. This result is astonishing, and indicates further potential for the synthesis of Mg based bimetallic NPs with various combinations of immiscible elements, which is still unexplored for hydrogen storage.

Fig. 2(a) & (c) show bright field TEM images of MgTi NPs produced using methane (CH$_4$) gas as an impurity/reactive gas once nucleation has stopped. The absence of nucleation was confirmed using the Quartz Crystal Microbalance (QCM) that indicated zero deposition rate. Moreover, under the same conditions, the sample does not show any NPs during TEM analysis, confirming the absence of NP nucleation. The NPs produced show a narrow size distribution with a core shell structure. The NPs consist of a 25 ± 3 nm core surrounded by a 12 ± 3 nm shell that as a whole is enclosed in a 3–4 nm thin MgO outer shell, resulting in a narrow monodisperse size distribution of 56 ± 3 nm. The NPs contain 85 ± 1 at% Mg and 15 ± 1 at% Ti overall excluding the carbon content and if we account for carbon then the core contains 9 ± 2 at% Mg, 60 ± 2 at% Ti and 31 ± 2at% C. Excluding Mg for the core, the amount of Ti and C is 66 ± 2 at% Ti and 34 ± 2 at% C in the core as measured by EDX. The detailed analysis of the core/shell structure from the single NP diffraction shown in Fig. 2(c) confirms FCC TiC as a core and HCP Mg as a shell. The resolved shape by TEM analysis is a truncated hexagonal pyramid compared to the hexagonal prismatic shape of (pure) Mg. The bright-field TEM image in Fig. 2(d) shows that both the TiC core and the Mg shell are faceted and share an epitaxial relationship with TiC{220}//Mg{11–20} and TiC{111}//Mg {0002}.

Furthermore, if we compare the resulting morphologies using methane and hydrogen, the NPs produced using hydrogen result in a solid solution, while methane results in phase
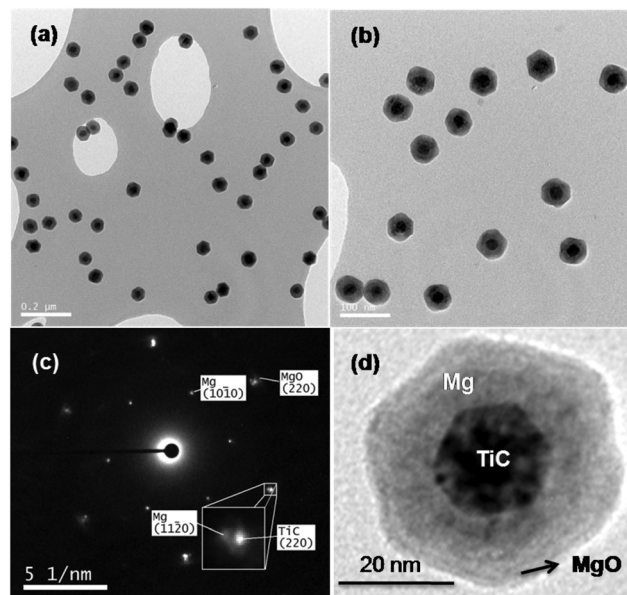

Fig. 2 Bright-Field TEM images of MgTi NPs produced using methane as a trace gas. (a, b) TiC/Mg core/shell NPs with a uniform size distribution at different magnifications. (c) Selected area diffraction pattern (SAED) of the TiC/Mg NP shown in Fig. 3(d). (d) High magnification TEM image showing the faceted TiC core and Mg shell.

separation and a core–shell structure. This can be attributed to the specific interaction of methane/hydrogen with metal atoms occurring in the plasma during the synthesis of NPs. In the case of CH_4, once it dissociates in the plasma,[24,25] Ti atoms interact with carbon to form a TiC core, as continuous supply of carbon and Ti is maintained during the synthesis. Furthermore, Ti affinity towards carbon is higher than that of Mg, and TiC formation is easier compared to MgC as is known from the phase diagram.[26–29] Once TiC grows, it acts as a nucleus for further Mg growth. Hence, it results in the formation of a core–shell structure. The above assumption is valid because of the issue of Mg nucleation, and the orientation relationship between TiC and Mg. The latter confirms that Mg grows on TiC forming a core shell structure. Therefore, the resulting structure is not due to segregation. Similarly, during interaction with hydrogen, TiH_x species act as nuclei to form MgTi NPs but with the formation of MgTi solid solution. Fig. 3 shows a schematic illustration of MgTi NP formation under these different conditions for ($\frac{1}{2}$ Mg + $\frac{1}{2}$ Ti) section target composition.

Fig. 4(a) shows a bright-field TEM image of the NPs based on a 50%Mg–50%C section target synthesized using CH_4 as an impurity/trace gas. The purpose of using the Mg–C combination was to verify whether carbon may favor nucleation of Mg similarly to MgTi. However, without CH_4 addition, nucleation was not at all observed. Moreover, after adding CH_4, the nucleation and production of NPs was initiated successfully. Electron diffraction analysis, which is shown in Fig. 4(b), confirms the presence of Mg NPs, as interplanar distances match with pure Mg and indicate non-solubility of carbon and solid solution formation under the present conditions. From the phase diagram,[27,28] carbon solubility in Mg is negligible even in the liquid state, indicating an improbable Mg–C formation. Fig. 4 shows the as prepared 'Mg–C' NPs with a morphology that is distinctly different from the hexagonal prismatic shape of (pure) Mg, still indicating that the methane/carbon impurities did influence the formation of the resulting Mg NPs. This may be due to insufficient time for the Mg–C particles to coalesce during NP formation, as observed previously for Cu–C NP formation.[25] In addition, depending on carbon's concentration and its specific adsorption in the planes at a faster growth rate, it can reduce the growth rate of that plane by affecting the kinetics and particle shape formation.[30] Also, carbon adsorbed on the surface of the NPs can prevent particle coalescence and, therefore, affect the final NP morphology.

In contrast to MgTi NPs, we did not observe the issue of nucleation for MgNi and MgCu NPs reported in our previous article.[11] To explore this further, and to observe the effect of combining elements during NP synthesis, we chose the MgPd system, where Pd is a noble metal and is easy to nucleate. Fig. 5(a) & (b) show the bright-field TEM and HAADF-STEM images of the MgPd NPs. The NPs produced show a homogeneous interior indicating similarity to a solid solution; in particular, the Z-contrast sensitive image in Fig. 5(b) indicates
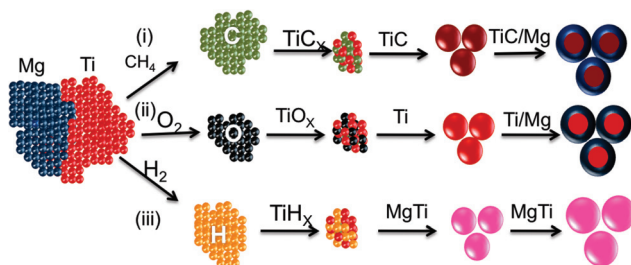

Fig. 3 Schematic illustration of MgTi NP nucleation and formation using the section target ($\frac{1}{2}$Mg + $\frac{1}{2}$ Ti) under various conditions. (i, iii) The effect of a trace level of methane and hydrogen on the MgTi NP formation. (i) The core shell TiC/Mg structure in comparison with (iii), which shows the solid solution MgTi formation for the same concentration level of methane and hydrogen. (ii) MgTi NP formation in the absence of methane and hydrogen with a trace level of oxygen impurity present in the aggregation zone of NP synthesis or adsorbed on the target prior to the deposition.
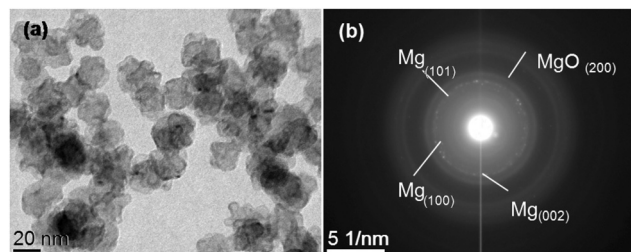

Fig. 4 (a) Bright-Field TEM image of the MgC NPs produced at 0.250A using ($\frac{1}{2}$Mg + $\frac{1}{2}$C) section target. (b) Electron diffraction pattern confirming the presence of Mg.
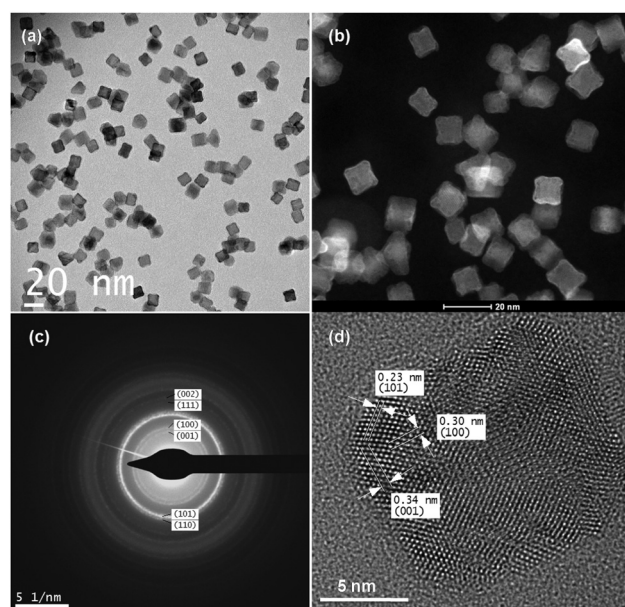

Fig. 5 (a) Bright-field TEM image of MgPd NPs produced at 0.250A using ($\frac{1}{2}$Mg + $\frac{1}{2}$C) section target. (b) HAADF-STEM image of the MgPd NPs. (c) Electron diffraction pattern confirming the tetragonal structure of the MgPd NPs. (d) HRTEM image of an MgPd NP.

homogeneous particles. The selected area electron diffraction (SAED) pattern shown in Fig. 5(c) shows that the structure of the MgPd NPs exhibits a tetragonal crystal lattice with lattice parameters of a = 0.310 nm and c = 0.351 nm. This crystal structure was verified using the HRTEM images shown in Fig. 4(d), where the (100), (001) and (101) planes are resolved. Indeed, viewing along the [100] zone axis, the orthogonal (100) and (001) planes are resolved, which are parallel to the particle's facets.

A detailed analysis of HRTEM images reveals the presence of a body centered tetragonal lattice that corresponds to the $Mg_{0.9}Pd_{1.1}$ intermetallic structure that has lattice parameters of a = 0.303 nm and c = 0.342 nm. This intermetallic structure occurs near a composition of 55 at% Pd. The MgPd intermetallic shows an ordered structure equivalent to the ordered AuCu lattice, where alternating Au and Cu layers are formed along the c-axis. Therefore, the body centered tetragonal structure most likely consists of alternating Mg and Pd (002) planes. These alternating planes ensure that the (100) and (001) spots cannot be fully cancelled and therefore are still visible in the SAED pattern. In comparison with MgTi NP synthesis, MgPd did not show any issues in nucleation and NP production. The latter shows that Pd can easily nucleate itself under the synthesis conditions. This observation is corroborated by the fact that during the start to the end of deposition, the nucleation and deposition rates did not change. The behavior was the same for the different samples produced using MgPd. Here, we cannot completely exclude the fact that impurities like O_2 or C are not present during nucleation and not affecting the nucleation; therefore more in-depth understanding is required. Nevertheless, our further analysis confirms that by introducing H_2 we can also nucleate and form a solid solution with MgPd. Since Pd can absorb hydrogen, it can easily form PdH_x species that could favor nucleation.

In the case of MgTi, venting the system (where the possibility of impurities being adsorbed on the target/aggregation volume is high) after each deposition did not influence the nucleation. In fact, the nucleation was completely blocked for the next successive depositions without any trace gas. Therefore, the amount of impurities present on the target prior to each deposition plays a major role in the nucleation process, and is more crucial compared to the impurities present in the gas phase growth region. Therefore, each time we supply H_2/CH_4, these molecules dissociate in the plasma and poison the target to the right proportion (depending on the concentration/amount of H_2/CH_4 gas introduced), so that the nucleation process starts and sustains for the entire duration of deposition. The indirect evidence of this can be inferred from the rise in voltage during the constant current mode operation of the sputtering process and NP production. Our modified sample holder assembly with five TEM sample slots allows us to identify the structural and compositional changes that occur during the continuous process of NP synthesis within the same deposition process.

To understand in depth the nucleation issue, we have to find the key variables that influence the nucleation conditions and play an important role in NP synthesis. According to our experimental observations and from our qualitative analysis, we find that the dimer binding energy/bond energy and the vapor pressure of elements are two important factors affecting the nucleation. In the case of Mg and Ti, the Mg–Mg binding energy is 0.088 eV, that for Ti–Ti is 1.219 eV, that for Ti–O is 6.908 eV, and that for Mg–O is 3.712 eV.[16,31,32] It is evident from these energies that homogeneous nucleation of Mg is rather difficult as the nuclei will not be stable to form stable critical nuclei. Under these conditions, impurities like O_2 in the plasma can form TiO_x or MgO_x species that have a higher dimer binding energy to form stable nuclei. Since TiO_x species are more stable and easy to form compared to MgO_x, Ti starts to nucleate on them first and later Mg grows on Ti. Under these conditions, TiO_x is not able to grow as a TiO core due to the lack of oxygen atoms, but the formation of a Ti core is favored due to continuous supply of Ti atoms during sputtering. Moreover, Ti is an acceptor of oxygen atoms and therefore it will consume oxygen rather quickly.

Furthermore, if we compare the vapor pressures, Mg has high vapor pressure compared to Ti for all conditions, and will favor destabilization of the nuclei affecting formation of NPs. In addition, Mg also has higher affinity for oxygen, so by introducing O_2 as a trace gas it will transform into MgO NPs more predominantly than form Mg NPs, and controlling the right concentration of O_2 will be rather difficult. In order to simplify this, we have introduced CH_4 and H_2 as trace gases for the synthesis of MgTi NPs. Note that the dimer binding energies of Mg–H, Ti–H, Ti–C and Mg–C are 1.345, 2.114, 4.384 and 1.520 eV,[31,32] respectively. This indicates that with CH_4 as an impurity gas, the formation of TiC_x nuclei is favored. These are more stable and grow with the continuous supply of carbon to form the TiC core for the subsequent Mg growth.

Similarly, with H_2 as a trace/impurity gas the formation of TiH_x nuclei is favored, which has a favorable binding energy as compared to MgH_x. In general, both Ti and Mg have a strong affinity for hydrogen, and thermodynamically Mg is also favorable for MgH formation. However, kinetics is a limiting factor for MgH formation compared to TiH during the synthesis. This is similar to the observation on TiH_2 over MgH formation under the hydrogen plasma metal reaction (HPMR) reported earlier for ultra-fine nanoparticles. Therefore, we could justify the fact that stable TiH_x species form first, and Ti and Mg grow on them. Furthermore, the presence of hydrogen, and its absorption during the nuclei formation, induces a lot of defects, e.g. vacancies in the NP that will allow Ti atoms to diffuse and occupy the vacant sites to form a solid solution/alloy. Moreover, a similar observation is also reported for Pd–Au NPs in creating alloy structures in the presence of hydrogen.[33] This is an interesting observation and further investigations are required to understand in detail the effect of H_2 on alloy formation.

Nonetheless, NP formation based on Mg/C section targets did not occur unless CH_4 was introduced. This clearly indicates that carbon atoms sputtered from the target did not favor the formation of MgC_x species that could act as nuclea-

tion centers for Mg growth. In comparison with Mg, the carbon sputtering yield is low (0.25 as compared to 3.6 at 500 eV) showing that nucleation of MgC_x species in the formation of Mg nanoparticles becomes unfavorable. But as soon as CH_4 is introduced, nucleation occurs without any limitation. The dimer binding energies of Mg–H and Mg–C are 1.345 eV and 1.520 eV, which are nearly equal to each other, but carbon does not favor the nucleation under the synthesis conditions. It is evident from the above that the hydrogen dissociated from CH_4 in the plasma can only react with Mg to form MgH_x species that favors the formation of Mg NPs. The concentration of methane supplied as a trace gas is only sufficient to initiate and maintain the nucleation process of Mg–C NPs and does not contribute to the formation of MgH_2 as the kinetics under the present conditions is limited for MgH_2 growth.

In the case of MgPd, the binding energies of Pd–Pd, Pd–H, Pd–C, Pd–O are 1.430, 2.425, 4.519 and 2.467 eV, respectively, which indicates that the presence of impurities and/or introduction of CH_4 or H_2 can favor Pd nucleation. However, without the contribution of any impurity, nucleation of Pd can occur only by self-nucleation or by Mg–Pd nucleation as Mg and Pd can from a strong bond. Moreover, we did not observe the formation of a Pd core acting as a nucleation center for Mg growth as compared to MgTi, MgNi and MgCu NPs under the same synthesis conditions that only show core/multi-shell structure formation. Furthermore, the composition of MgPd from the structure analysis is nearly 50% atomic concentration for Mg and Pd matching with sputtering yields of Mg and Pd (3.6 *vs.* 3.3)[34] that are nearly the same. Furthermore, if we compare the NPs of MgNi, MgCu and MgPd during synthesis, it emerges as a common observation that after each deposition the system was vented to transfer the sample for further TEM analysis. This provides the possibility for target poisoning and contamination of aggregation volume with trace elements like O_2, H_2O, *etc.* Nevertheless, in the case of MgTi synthesis, multiple system venting did not influence the NP nucleation. Therefore, we can conclude that the Ti diatomic binding energy with O is very high as compared to NiO, CuO and PdO: 6.908 *vs.* 3.793, 2.975, and 2.467 eV,[16,32] respectively, which implies that the consumption of O_2 by Ti is very rapid, thus terminating any further nucleation (while for the other elements the O consumption is slower). Moreover, the sputtering yields and monoatomic binding energies of Ni (2.00, 2.74 eV), Cu (2.6, 2.083 eV) and Pd (3.3, 1.5 eV) are high as compared to Ti (0.46, 1.219 eV),[34] which leads to higher probability of cluster formation in addition to impurity-assisted nucleation.

Finally, with our modified sample holder that supports five TEM samples and the possibility of depositing one sample at a time, we produced MgNi NPs and collected the NPs on different TEM samples at different intervals of the same deposition. It was observed that the production rate started to drop after 30 min but did not come to a halt as in the case of MgTi. The samples deposited at different interval show variation in composition and size distribution. These observations indicate that impurities present in the system still play a major role in nucleation, even if (it seems that) homogeneous nucleation is possible, thereby affecting the production rate/yield. This clearly concludes that depositions of MgNi, MgCu and MgPd based on short(er) time intervals, and venting the system for sample exchange, favor subsequent production of NPs without any nucleation problem. Moreover, self-nucleating elements like Pd, Ni and Cu can favor Mg based bimetallic NP synthesis but continuation of deposition for prolonged duration and making large quantities will be an issue without the addition of impurities.

Conclusions

In summary, we have shown that the introduction of trace amounts of CH_4 or H_2 and the addition of a self-nucleating element (*e.g.* Pd) can be used as a strategy to solve the formidable problem of bimetallic NP nucleation in the gas phase. The synthesized MgTi NPs show different structural motifs, a phase separated TiC/Mg core shell in the case of CH_4 and a solid solution in the case of H_2. Addition of a self-nucleating element like Pd to Mg can initiate and sustain the nucleation with or without the addition of a trace gas. We have explained the issue of bimetallic NP nucleation and formation of various structures in the presence of impurity/trace gases using the dimer binding energy of each element. Moreover, a better control of the NP production, together with an increase in NP production rate/yield and a more uniform NP size distribution, has been achieved using impurity/trace gases. This opens up the possibility of scaling up NPs for different applications as gas-phase condensation based on sputtering can overcome the limitation of making only small quantities of NPs. Finally, the same strategies presented here can also be applied and extended for the synthesis of more complex multicomponent NPs. Although both H_2 and CH_4 can assist in NP synthesis, H_2 promises to be more beneficial in synthesizing the structure of interest. Nevertheless, the trace gas can be preselected according to the element interactions (dimer binding energies) and structure/morphology of interest.

Experimental methods

Synthesis

The MgTi, MgC and MgPd bimetallic nanoparticles with various structures were produced by a home modified nanoparticle system, Nanogen 50 from Mantis Deposition Ltd (http://www.mantisdeposition.com). The sample chamber was evacuated to a base pressure of $\sim 1 \times 10^{-8}$ mbar and an oxygen partial pressure of $\sim 10^{-11}$ mbar. Supersaturated metal vapor was produced by magnetron sputtering of a sectioned target (99.95% purity Mg, C, Pd and Ti obtained from Alpha Aesar) shown in Fig. S1 of the ESI† at an inert argon atmospheric pressure of ~ 0.25 mbar and 0.250 A discharge current. The supersaturated metal vapor was then cooled using argon gas in order to form nuclei, which could subsequently grow into

nanoparticles. The nanoparticles formed in the aggregation volume were removed fast by the use of argon that acts as a drift and sputter gas. CH_4/H_2 trace gas was introduced, by means of a high precision UHV-leak valve, directly into the aggregation chamber up to a pressure of $\sim 6 \times 10^{-4}$ mbar (or less). Direct measurement of the CH_4/H_2 partial pressure during sputtering was not feasible because the magnetron is operated at a high Ar pressure for sputtering (0.25 mbar).

TEM analysis

The nanoparticles transported from the aggregation volume were deposited onto 25 nm thick Si-nitride membranes or carbon coated Cu grids, which were used for Transmission Electron Microscopy (TEM) analysis on a JEOL 2010F TEM. In particular, MgPd TEM and STEM imaging was performed using the double corrected, monochromated high brightness Titan[3] 60–300 at an accelerating voltage of 300 kV for the best spatial resolution (<70 pm in TEM and STEM). HAADF-STEM imaging was performed with 21.5 mrad convergence semiangle, a probe current of <10 pA and detector acceptance angles between 80–250 mrad.

Acknowledgements

References

1 K. D. Gilroy, A. Ruditskiy, H. Peng, D. Qin and Y. Xia, *Chem. Rev.*, 2016, **116**, 10414–10472.

2 S. Duan and R. Wang, *Prog. Nat. Sci.: Mater. Int.*, 2013, **23**, 113–126.

3 R. G. Chaudhuri and S. Paria, *Chem. Rev.*, 2012, **112**, 2373.

4 M. Cargnello, R. Agarwal, D. R. Klein, B. T. Diroll, R. Agarwal and C. B. Murray, *Chem. Mater.*, 2015, **27**, 5833.

5 L. Carbonea and P. D. Cozzoli, *Nano Today*, 2010, **5**, 449.

6 X. Liu, D. Wang and Y. Li, *Nano Today*, 2012, **7**, 448–466.

7 G. Krishnan, M. A. Verheijen, G. H. ten Brink, G. Palasantzas and B. J. Kooi, *Nanoscale*, 2013, **5**, 5375–5383.

8 G. E. Johnson, R. Colby and J. Laskin, *Nanoscale*, 2015, **7**, 3491–3503.

9 M. Benelmekki, J. Vernieres, J.-H. Kim, R.-E. Diaz, P. Grammatikopoulos and M. Sowwan, *Mater. Chem. Phys.*, 2015, **151**, 275–281.

10 M. Benelmekki, J. Vernieres, J. Kim, R. Diaz, P. Grammatikopoulos and M. Sowwan, *Mater. Chem. Phys.*, 2015, **151**, 275–281.

11 G. Krishnan, R. F. Negrea, C. Ghica, G. H. ten Brink, B. J. Kooi and G. Palasantzas, *Nanoscale*, 2014, **6**, 11963–11970.

12 D. Llamosa, M. Ruano, L. Martinez, A. Mayoral, E. Roman, M. Garcia-Hernandez and Y. Huttel, *Nanoscale*, 2014, **6**, 13483–13486.

13 M. Benelmekki, M. Bohra, J. Kim, R. E. Diaz, J. Vernieres, P. Grammatikopoulos and M. Sowwan, *Nanoscale*, 2014, **6**, 3532–3535.

14 D. L. Olynick, J. M. Gibson and R. S. Averback, *Appl. Phys. Lett.*, 1996, DOI: 10.1063/1.116710.

15 D. L. Olynick, J. M. Gibson and R. S. Averback, *Philos. Mag. A*, 1998, **77**, 1205–1221.

16 T. Peter, O. Polonskyi, B. Gojdka, A. Mohammad Ahadi, T. Strunskus, V. Zaporojtchenko, H. Biederman and F. Faupel, *J. Appl. Phys.*, 2012, DOI: 10.1063/1.4768528.

17 T. Acsente, R. F. Negrea, L. C. Nistor, C. Logofatu, E. Matei, R. Birjega, C. Grisolia and G. Dinescu, *Eur. Phys. J. D*, 2015, **69**, 161.

18 O. Polonskyi, O. Kylián, M. Drábik, J. Kousal, P. Solař, A. Artemenko, J. Čechvala, A. Choukourov, D. Slavínská and H. Biederman, *J. Mater. Sci.*, 2014, **49**, 3352–3360.

19 A. Marek, J. Valter, S. Kadlec and J. Vyskočil, *Surf. Coat. Technol.*, 2011, **205**(Supplement 2)), S573–S576; *PSE 2010 Special Issue Proceedings of the 12th International Conference on Plasma Surface Engineering*.

20 G. Krishnan, B. J. Kooi, G. Palasantzas, Y. Pivak and B. Dam, *J. Appl. Phys.*, 2010, DOI: 10.1063/1.3305453.

21 G. Krishnan, G. Palasantzas and B. J. Kooi, *Appl. Phys. Lett.*, 2010, DOI: 10.1063/1.3533812.

22 B. J. Kooi, G. Palasantzas and J. T. M. De Hosson, *Appl. Phys. Lett.*, 2006, DOI: 10.1063/1.2358860.

23 I. J. T. Jensen, O. M. Løvvik, H. Schreuders, B. Dam and S. Diplas, *Surf. Interface Anal.*, 2012, **44**, 986–988.

24 A. Majumdar, J. Behnke, R. Hippler, K. Matyash and R. Schneider, *J. Phys. Chem. A*, 2005, **109**, 9371–9377.

25 G. H. ten Brink, G. Krishnan, B. J. Kooi and G. Palasantzas, *J. Appl. Phys.*, 2014, DOI: 10.1063/1.4895483.

26 Y.-J. Kim, H. Chung and S.-J. L. Kang, *Composites, Part A*, 2001, **32**, 731–738.

27 H. Chen and R. Schmid-Fetzer, *IJMR*, 2012, **103**, 1294–1301.

28 B. Predel, C–Mg (Carbon–Magnesium), in *Landolt-Börnstein Group IV Physical Chemistry*, Springer-Verlag, Berlin, Heidelberg, 2012, vol. 12B, p. 138, DOI: 10.1007/978-3-540-44756-6_94.

29 B. Predel, C–Ti (Carbon–Titanium), in *Landolt-Börnstein Group IV Physical Chemistry*, Springer-Verlag, Berlin, Heidelberg, 2012, vol. 12B, pp. 147–149, DOI: 10.1007/978-3-540-44756-6_102.

30 D. E. Grove, U. Gupta and A. W. Castleman, *ACS Nano*, 2010, **4**, 49–54.

31 F. Ruette, M. Sánchez, R. Añez, A. Bermúdez and A. Sierraalta, *J. Mol. Struct.: THEOCHEM*, 2005, **729**, 19–37;

Proceedings of the 30th International Congress of Theoretical Chemists of Latin Expression, The 30th International Congress of Theoretical Chemists of Latin Expression.

32 Y. Luo, *Comprehensive Handbook of Chemical Bond Energies*, Taylor & Francis, CRC Press, 2007.

33 H. Kobayashi, M. Yamauchi, R. Ikeda and H. Kitagawa, *Chem. Commun.*, 2009, 4806–4808.

34 SPUTTERING YIELD VALUES, http://www.npl.co.uk/science-technology/surface-and-nanoanalysis/.../sputter-yield-values (accessed November/Friday 2016).